

See discussions, stats, and author profiles for this publication at: <https://www.researchgate.net/publication/234097636>

Functionalization of Graphite Oxide with Magnetic Chitosan for the Preparation of a Nanocomposite Dye Adsorbent

ARTICLE in LANGMUIR · JANUARY 2013

Impact Factor: 4.46 · DOI: 10.1021/la304696y · Source: PubMed

CITATIONS

74

READS

176

4 AUTHORS:



Nikolina A Travlou

Aristotle University of Thessaloniki

15 PUBLICATIONS 182 CITATIONS

[SEE PROFILE](#)



George Kyzas

Technological Educational Institute of Kavala

59 PUBLICATIONS 1,114 CITATIONS

[SEE PROFILE](#)



Nikolaos K Lazaridis

Aristotle University of Thessaloniki

100 PUBLICATIONS 2,420 CITATIONS

[SEE PROFILE](#)



Eleni A Deliyanni

Aristotle University of Thessaloniki

57 PUBLICATIONS 1,265 CITATIONS

[SEE PROFILE](#)

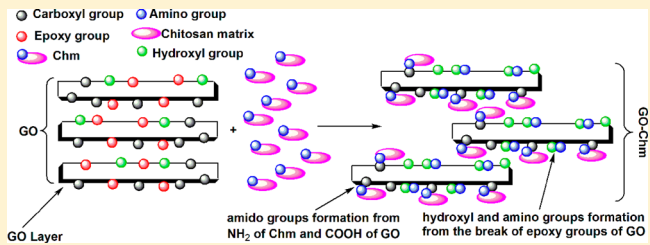
Functionalization of Graphite Oxide with Magnetic Chitosan for the Preparation of a Nanocomposite Dye Adsorbent

Nikolina A. Travlou, George Z. Kyzas, Nikolaos K. Lazaridis, and Eleni A. Deliyanni*

Laboratory of General & Inorganic Chemical Technology, Division of Chemical Technology, School of Chemistry, Aristotle University of Thessaloniki, GR-541 24 Thessaloniki, Greece

Supporting Information

ABSTRACT: In the current study, the functionalization of graphite oxide (GO) with magnetic chitosan (Chm) was investigated to prepare a nanocomposite material (GO–Chm) for the adsorption of a reactive dye (Reactive Black 5). The synthesis mechanism was investigated by various techniques (SEM/EDAX, FTIR spectroscopy, XRD, XPS, DTA, DTG, VSM). Characterization results indicated that a significant fraction of the amines of the chitosan (i) were inserted between the GO layers and (ii) reacted with carboxyl and epoxy groups of GO, leading to its reduction and hence the destruction of the layered structure. The concentrations of iron were found to be ~25% for Chm and ~12% for GO–Chm. A VSM plot presents the value of 9 emu/g for the saturation magnetization of GO–Chm. The adsorption behavior of the prepared composite was elucidated with a series of experiments. The tests of the effects of pH revealed that the adsorption mechanism dominated (between dye molecules and the GO–Chm matrix) and showed that acidic conditions were the optimum for the adsorption process (pH 3). Kinetic experiments presented the relatively “fast” adsorption phenomenon using pseudo-first-order, pseudo-second-order, and modified pseudo-second-order equations. The equilibrium data were fitted to the Langmuir, Freundlich, and Langmuir–Freundlich (L–F) models, calculating the maximum adsorption capacities at 25, 45, and 65 °C (391, 401, and 425 mg/g, respectively). Thermodynamic analysis was also performed to calculate the changes in free energy (ΔG°), enthalpy (ΔH°), and entropy (ΔS°).



1. INTRODUCTION

The release of dyes into the environment constitutes only a small proportion of water pollution, but dyes are visible in even small quantities because of their brilliance.¹ Most synthetic dyes are toxic and cannot be efficiently decolorized by traditional methods. The adsorption of synthetic dyes onto adsorbents is considered to be a simple and economical method for their removal from water and wastewater.² In particular, adsorption onto activated carbon appears to have the best prospect for eliminating dyes.³ Despite its good efficiency, this adsorbent is usually derived from wood or coal, which is considered expensive. Therefore, in recent years, many researches have focused on the use of various cheaper adsorbents instead of activated carbon. The new trends are focused on carbon- and polysaccharide-based materials.⁴

Graphene (Gh), a novel one-atom-thick two-dimensional graphitic carbon system, is a rising star in materials science and condensed-matter physics.⁵ Following this trend, graphite oxide (GO) has re-emerged as a research interest owing to its role as a precursor for the cost-effective mass production of graphene-based materials. GO has a layered structure similar to that of graphite, but the plane of carbon atoms in graphite oxide is heavily decorated by oxygen-containing groups, which can be exfoliated in water under moderate ultrasonication. If the exfoliated sheets contain only one or few layers of carbon atoms as in graphene, these sheets are called graphene oxide (GhO).

The latter can be reduced to graphene-like sheets by removing the oxygen-containing groups.⁶

Graphite oxide has been extensively studied and characterized by many researchers in the past decade, and a brief search of the literature revealed various treatments in its structure.^{7–9} Despite the vast collection of publications regarding graphene or graphite oxide, very few of them have dealt with the adsorption of dyes. Recently, GO was studied as an adsorbent, and its ability to remove cationic dyes (methyl violet, methyl green, and neutral red) was demonstrated.¹⁰ GO has multiple oxygen-containing functional groups (carboxyl, hydroxyl, epoxy) that can be covalently attached to its layers, resulting in a negatively charged surface.¹⁰ In other studies, GhO showed a removal efficiency of up to 95% for cationic dyes and an essentially negligible removal efficiency for anionic ones. Oppositely, the removal efficiency of Gh was reported to be 95% for anionic dyes and 50% for cationic dyes.^{4,11}

On the other hand, chitosan (Ch) is a multifunctional polymer that has primary and secondary hydroxyl groups, as well as highly reactive amino groups. It is regarded as a useful starting support for adsorption purposes. Numerous investigations on the chemical activation of chitosan have been

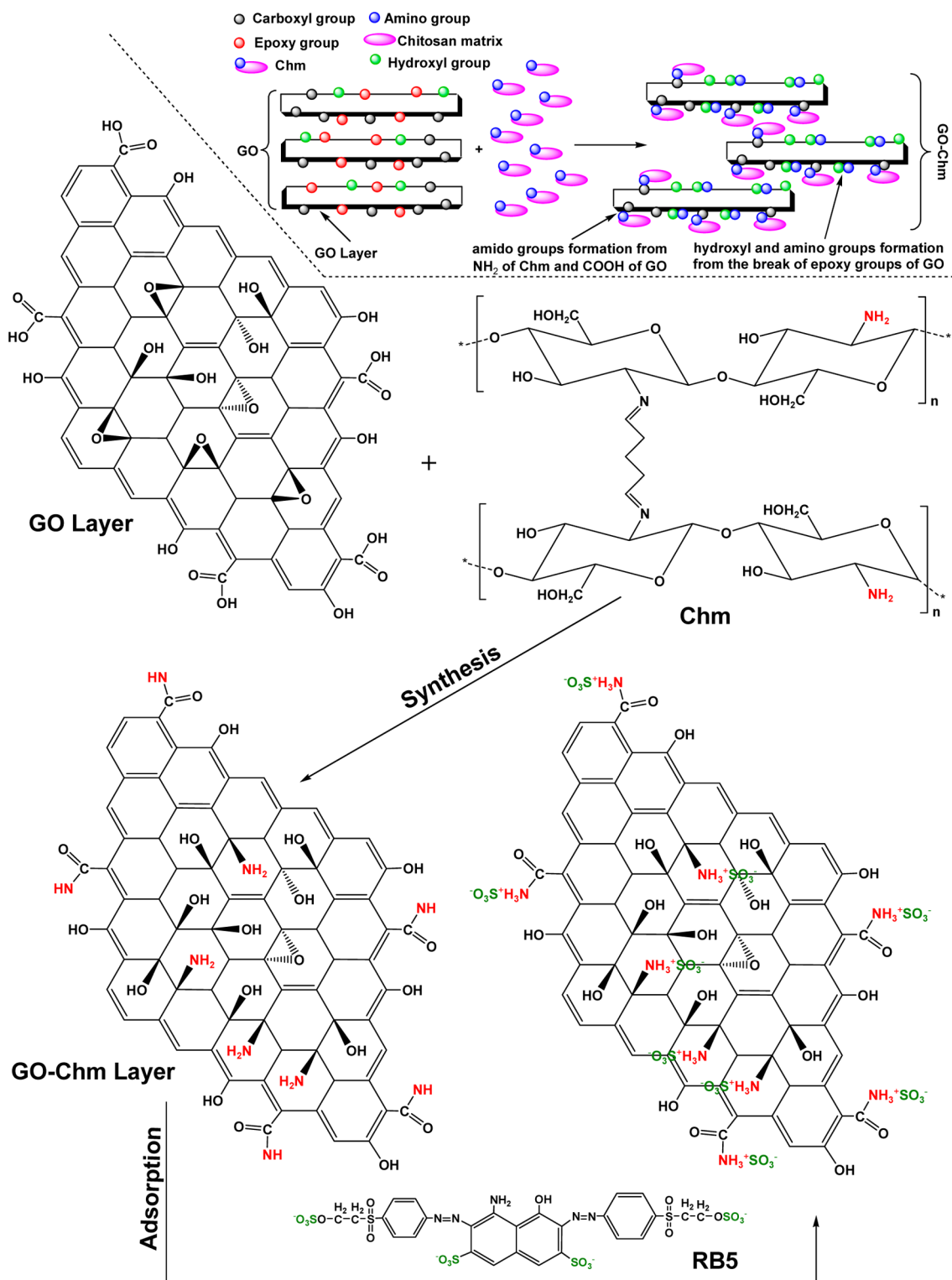
Received: November 26, 2012

Revised: January 8, 2013

Published: January 9, 2013



Scheme 1. Proposed Synthesis Mechanism of GO–Chm after Functionalization of Chm on GO and Proposed Mechanism of RB5 Adsorption onto the Prepared GO–Chm



carried out to increase its adsorption capacity for dyes.¹² In fact, magnetic chitosan has emerged as one of a new generation of materials for environmental decontamination, because magnetic separation involves the simple application of an external magnetic field to extract the adsorbents. Compared with traditional methods, such as filtration, centrifugation, or gravitational separation, magnetic separation requires less

energy and can achieve better separation (especially for adsorbents with small particle sizes).^{13–15}

The novelty of the current study involves two aspects. (i) First, the proposed mechanism of synthesis of the nanocomposite is the functionalization of graphite oxide and magnetic chitosan. This mechanism was explained by different characterization techniques [scanning electron microscopy/

energy-dispersive analysis by X-rays (SEM/EDAX), Fourier transform infrared (FTIR) spectroscopy, X-ray powder diffraction (XRD), X-ray photoelectron spectroscopy (XPS), differential thermal analysis (DTA), differential thermal gravimetry (DTG)], which revealed a novel interaction between the epoxy groups of graphite oxide and the amino groups of chitosan. (ii) Second, the adsorption of the composite prepared with a series of dye adsorption–desorption experiments was evaluated by studying the main parameters of the process (pH, initial dye concentration, contact time, temperature) along with a thermodynamic analysis. This adsorption evaluation illustrated the impressive enhancement of the maximum adsorption capacity of the nanocomposite prepared compared to that of GO.

2. EXPERIMENTAL SECTION

2.1. Materials. Chitosan of high molecular weight (Ch_{HMW}) was purchased from Sigma-Aldrich and purified by extraction with acetone in a Soxhlet apparatus for 24 h. Then, it was dried under a vacuum at 20 °C. Its average molecular weight was estimated at 3.55×10^5 g/mol, and the degree of deacetylation was 82 wt %.¹⁶ The cross-linking agent used was glutaraldehyde (GLA), which was obtained from Sigma-Aldrich (50 wt % in water). All solvents were of analytical grade. The reactive dye Reactive Black 5, C.I. 20505 (RBS), was used as the target molecule for adsorption experiments. The dye (supplied by Kahafix) presents the following characteristics: $\text{C}_{26}\text{H}_{21}\text{N}_5\text{Na}_4\text{O}_{19}\text{S}_6$, MW = 991.82 g/mol, $\lambda_{\text{max}} = 603$ nm, purity = 55% w/w. The dye purity was taken into account for all calculations. The chemical structure of the dye used is given in Scheme 1.

2.2. Synthesis of Adsorbents. **2.2.1. Synthesis of Magnetic Nanoparticles.** $\text{FeCl}_2 \cdot 4\text{H}_2\text{O}$ (3.5 g), $\text{FeCl}_3 \cdot 6\text{H}_2\text{O}$ (9.5 g), and 400 mL of doubly distilled water were stirred in a water bath at 60 °C under N_2 for 1 h. Ammonia solution was added dropwise, and the mixture was purged with nitrogen until it reached pH 10. The precipitate thus obtained was decanted in a dialysis tubing cellulose membrane (Sigma Co.), and the precipitate-coated membrane was placed in a bath filled with distilled water. The chloride ions present in the initial suspension were slowly removed by osmosis through the membrane. The presence of Cl^- ions in the water bath was tested with a AgNO_3 (0.1 M) solution. The water of the bath was replaced several times until no more chloride ions could be detected. The resulting cake on the membrane surface after decanting was freeze-dried in a bench freeze drier (Christ Alpha 1-4).

2.2.2. Synthesis of Magnetic Chitosan (Chm). Pure chitosan (Ch_{HMW} , 2 g) was dissolved in 400 mL of acetic solution (2% v/v). Then, 0.75 g of magnetic particles was added to the chitosan solution, and the mixture was sonicated for 30 min. Then, GLA (cross-linker) was added to the mixture solution to cross-link chitosan. Cross-linking was carried out because chitosan presents a high swelling degree in aqueous solutions. To overcome this problem, because a chitosan-based nanocomposite was used as the adsorbent in this study, the chitosan has to be cross-linked.^{17,18} Therefore, 15 mL of GLA (50 wt % in water) was added to the reaction flask, and the solution was vigorously stirred at 60 °C for 2 h. The precipitate was washed with ethanol and then distilled water and dried in a vacuum oven at 50 °C. The obtained product was magnetic chitosan (Chm).

2.2.3. Synthesis of Graphite Oxide (GO). GO was synthesized by the modified Hummers method.¹⁹ Commercial graphite powder (10 g) was stirred in concentrated sulfuric acid (230 mL, 0 °C). Then, potassium permanganate (30 g) was slowly added to the suspension. The rate of addition was controlled to prevent a rapid rise in the temperature of the suspension, which should be less than 20 °C. The reaction mixture was then cooled to 2 °C. After removal of the ice bath, the mixture was stirred at room temperature for 30 min. Distilled water (230 mL) was slowly added to the reaction vessel, with the temperature maintained at less than 98 °C. The dilute suspension was stirred for an additional 15 min and was further diluted with 1.4 L of distilled water, and then 100 mL of a 30 wt % solution of hydrogen

peroxide was added. The mixture was left overnight. The GO particles settled at the bottom were separated from the excess liquid by decantation. The remaining suspension was transferred to dialysis tubes (Sigma Co.). Dialysis was carried out until no precipitate of BaSO_4 was detected by addition of an aqueous solution of BaCl_2 . Then, the wet form of graphite oxide was separated by centrifugation. The gel-like material was freeze-dried, and a fine dark brown powder of the initial graphite oxide (GO) was obtained.

2.2.4. Synthesis of Graphite Oxide–Magnetic Chitosan Composite (GO–Chm). Pure chitosan (Ch_{HMW} , 2g) was dissolved in 100 mL of acetic solution (2% v/v), and the mixture was sonicated for 30 min. Then 0.75 g magnetic particles was added to the chitosan solution, and the mixture solution was stirred for 2 h. Next, 15 mL of GLA (50 wt % in water) was added to the reaction flask, together with 1.5 g of GO. The mixture was adjusted to pH 9–10 and was stirred at 80 °C for 1 h. The precipitate was washed with ethanol and then distilled water and dried in a vacuum oven at 50 °C. The final product (GO–Chm) was ground to a fine powder, with a size after sieving in the range of 75–125 μm .

2.3. Characterization Techniques. Scanning electron microscopy (SEM) images were obtained on a Zeiss Supra 55 VP electron microscope. The accelerating voltage was 15.00 kV, and the scanning was performed *in situ* on a sample powder. EDAX analysis was performed at magnification 10 K and led to maps of the elements and elemental analysis.

FTIR spectra of the samples were recorded on a Perkin-Elmer 2000 FTIR spectrometer using KBr disks prepared by mixing 0.5% of the finely ground carbon sample in KBr. A pellet made of pure KBr was used as the reference sample for background measurements. The spectra were recorded from 4000 to 400 cm^{-1} at a resolution of 4 cm^{-1} . The spectra presented were baseline-corrected and converted to transmittance mode.

Thermal analysis was carried out using a TA Instruments SDT thermal analyzer. The instrument had a heating rate of 10 K/min and a flow rate of nitrogen atmosphere equal to 100 mL/min. Approximately 25 mg of sample was used for each measurement.

X-ray powder diffraction (XRD) patterns were recorded on a Philips PW1820 diffractometer with $\text{Cu K}\alpha$ radiation for crystalline phase identification. The sample was scanned from 20° to 80°.

Magnetic properties were measured on a vibrating sample magnetometer (VSM) at room temperature.

Photoemission experiments were carried out in an ultra-high-vacuum (UHV) system with a base pressure 1×10^{-9} mbar. The unmonochromatized $\text{Al K}\alpha$ line at 1486.6 eV and an analyzer pass energy of 97 eV, giving a full width at half-maximum (abbreviated as fwhm) of 1.7 eV for the $\text{Au } 4f_{7/2}$ peak, were used in all XPS measurements. The XPS core-level spectra were analyzed by decomposing each spectrum into individual mixed Gaussian–Lorentzian peaks after a Shirley background subtraction. The measurement errors for the XPS core-level peaks were estimated for a good signal-to-noise ratio, and the errors in peak positions were about ± 0.1 eV. The binding-energy scale was calibrated by assigning the main C 1s peak at 284.8 eV. The calibration of the analyzer's kinetic energy scale was done according to standard method ASTM E902-88.²⁰

2.4. Adsorption–Desorption Procedure. Batch adsorption experiments were carried out in 50 mL flasks, where $m = 0.020$ g of the adsorbent and $V = 20$ mL of RBS aqueous solutions of different initial concentrations were added in the presence of constant background electrolyte $I = 1$ M NaCl at pH 3. The flasks were placed in a reciprocating water bath shaker (Julabo SW-21C) in a controlled-temperature environment ($\Theta = 25$ °C) and mixed at a constant agitation rate ($N = 160$ rpm) for 24 h. Desorption experiments were realized by mixing the collected amount of dye-loaded adsorbents, after adsorption, with 20 mL (same volume as in the adsorption step) of deionized water as the eluent over a pH range of 3–12 [pH was adjusted by the addition of acid (HCl) or base (NaOH)], under conditions that were otherwise the same as for adsorption.

The effect of pH on the equilibrium uptake of dye was investigated in the pH range of 3–12. The initial pH values were adjusted with 0.1 M HCl or 0.1 M NaOH.

The effect of contact time (kinetics) on dye adsorption was investigated in the time scale of 0–24 h. The transient concentration (C_t) of the dye was analyzed by pseudo-first-order, pseudo-second-order, and modified pseudo-second-order equations.²¹

The effects of the initial dye concentration and temperature were determined for initial RBS concentrations ($[RBS]_0$) of 0–1000 mg/L and system temperatures (Θ) of 25, 45, and 65 °C. The resulting equilibrium data (C_e) were fitted to the Langmuir,²² Freundlich,²³ and Langmuir–Freundlich (L–F) isotherm models.²⁴

Aliquots were taken from the supernatant during the batch adsorption process, and the residual dye concentration of each solution was determined by measuring its absorbance using a double-beam UV-vis spectrophotometer (Hitachi, model U-2000) at 603 nm. The absorbance was converted to concentration using a calibration curve. The equilibrium amount, Q_e (mg/g), of adsorbed RBS in the solid phase was calculated using the mass balance equation $Q_e = (C_0 - C_e) \times (V/m)$.

2.5. Thermodynamics. A thermodynamic analysis was realized based on the equilibrium data for isotherms at three different temperatures, calculating the respective parameters (ΔG^0 , ΔH^0 , ΔS^0). The Gibbs free energy change (ΔG^0 , kJ/mol) of the adsorption process is expressed by the van't Hoff equation (eq 1),²⁵ based on the prior calculation (eq 2) of the equilibrium constant (K_c)

$$\Delta G^0 = -RT \ln(K_c) \quad (1)$$

$$K_c = \frac{C_s}{C_e} \quad (2)$$

where C_s (mg/L) is the amount adsorbed on the solid at equilibrium and R (= 8.314 J/mol K) is the universal gas constant.

The change in entropy [ΔS^0 , kJ/(mol K)] and the heat of adsorption (ΔH^0 , kJ/mol) at a constant temperature T (K) were calculated from the equation

$$\Delta G^0 = \Delta H^0 - T\Delta S^0 \quad (3)$$

From eqs 1–3, one can write

$$\ln(K_c) = \left(-\frac{\Delta H^0}{R} \right) \frac{1}{T} + \frac{\Delta S^0}{R} \quad (4)$$

The values of ΔH^0 and ΔS^0 were calculated from the slope and intercept, respectively, of a plot of $\ln(K_c)$ versus $1/T$.

3. RESULTS AND DISCUSSION

3.1. Characterization, Functionalization, Interactions.

The XRD patterns of Chm and GO–Chm are shown in Figure 1, indicating the presence of magnetite particles (Fe_3O_4). The six characteristic peaks of Fe_3O_4 at $2\theta = 30.1^\circ$, 35.5° , 43.3° , 53.4° , 57.2° , and 62.5° , attributable to the indices (220), (311), (400), (422), (511), and (440), respectively, were observed in both samples and indexed using the Joint Committee on Power Diffraction Standards database (JCPDS 19-0629) with a cubic inverse spinel structure.²⁶ The results showed that chitosan binding did not result in a phase change in the structure of the magnetic nanoparticles.

The average crystallite size, D (nm), of magnetite was calculated using the Debye–Scherrer equation²⁷

$$D = \frac{K_s \lambda}{B \cos \theta} \quad (5)$$

where K_s is a constant ($K_s = 0.9$ for Cu $K\alpha$ radiation), λ (nm) is the wavelength (0.15405 nm for Cu $K\alpha$ radiation), B is the peak width at half-maximum (rad), and θ is the diffraction

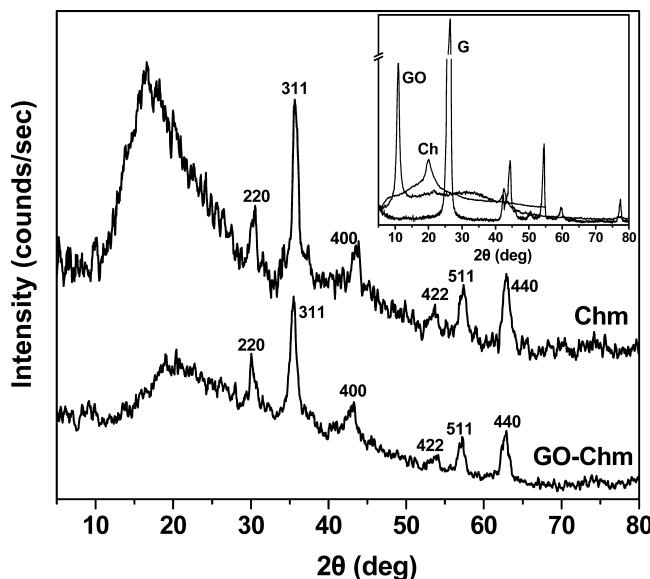


Figure 1. X-ray diffraction (XRD) patterns of Chm and GO–Chm. Inset: XRD patterns of Ch, GO, and G.

angle. The resulting crystallite size of magnetite in both samples was about 10.5 nm.

The patterns of Chm and GO–Chm also exhibited a broad peak at $2\theta = 20.3^\circ$ due to the presence of chitosan.²⁸ In the inset of Figure 1, the X-ray diffraction spectrograms of G, GO, and pure chitosan are presented. In the case of GO, the characteristic peak appeared at $2\theta = 11.3^\circ$, indicating an 8.11-Å estimated interlayer distance between the carbon layers, as determined by Bragg's law, which is clearly increased from the 3.36-Å interlayer distance for graphite. This is caused by the large amount of polar groups generated between the layers of graphite during oxidation,^{29,30} in which the oxygen and carbon atoms are covalently bonded, leading to an increase in the graphite's crystal lattice length along axis c .

In the XRD pattern of the GO–Chm composite, the presence of GO is not clearly demonstrated, although there is a small peak at $2\theta = 9^\circ$. This indicates that most of the graphite oxide was exfoliated/reduced upon reacting with chitosan, leading to structural disorder. Taking into account that a primary aliphatic amino nucleophilic substitution reaction on the epoxy groups of GO was the main insertion pathway between the graphite layers and that the insertion of the amino molecules induced changes in the basal spacing of GO with respect to their chain length,³¹ the XRD results indicate that a significant fraction of the amines of the chitosan (i) were inserted between the GO layers and (ii) reacted with the carboxyl and epoxy groups of GO, leading to its reduction and, hence, the destruction of the layered structure (Scheme 1). Changes in the basal spacing and exfoliation of the layered structure of GO have also been documented upon the insertion of large organic ammonium ions,^{32–34} as well as polyaniline, between the layers of graphite.³⁵

Figure 2a shows a typical SEM image of GO, which presents a sheetlike structure with large thickness, smooth surface, and wrinkled edge. The image of magnetic chitosan (Figure 2b) presents aggregation and spherical shape.^{36,37} It is concluded that chitosan was immobilized on the surface of Fe_3O_4 particles and that the construction of the magnetic chitosan was core–shell with an average diameter about 1 μ m as estimated from the SEM image. The GO–Chm nanocomposite had a much

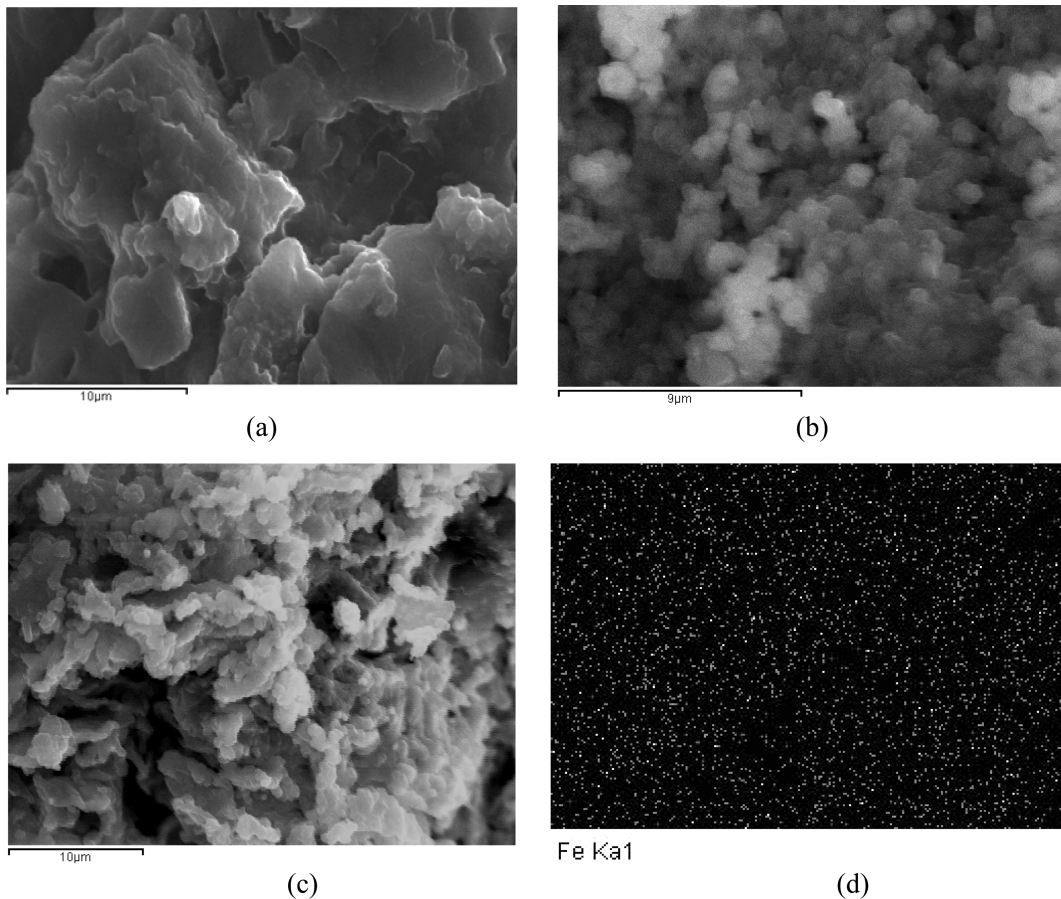


Figure 2. SEM images of (a) GO, (b) Chm, and (c) GO–Chm. (d) Iron distribution map of GO–Chm.

rougher surface, revealing that many small magnetic chitosan particles had been assembled on the surface of the GO layers with a high density.

Confirmation of the success of the chitosan coating process and the chemical compositions of the Chm and GO–Chm particles were determined by EDX analysis. The concentration of iron was found ~25% and ~12 for Chm and GO–Chm, respectively. This finding is consistent with the percentage of magnetic chitosan in the composite. The elemental percentage of carbon was 52% and 60%, and that of oxygen 22% and 25% for Chm and GO–Chm, respectively.

VSM was employed to study the magnetic properties of the synthesized material. Figure 3 shows the demagnetization curve of GO–Chm nanocomposite. The VSM plot presents a value of 9 emu/g for the saturation magnetization of the nanocomposite. This value is far less than that reported for pure magnetite colloidal nanocrystals, 36.941 emu/g.³⁸ This difference can be attributed to the rather small size of the Fe₃O₄ magnetite particles and the relatively low amount of Fe₃O₄ loaded on GO–Chm.^{39,40} However, the magnetic property remained high enough to meet the needs for magnetic separation. This fact can be clearly observed in the inset of Figure 3. The flask on the left contains an aqueous solution of RB5 (before adsorption), whereas the flask on the right contains the same solution after adsorption of RB5 onto GO–Chm. In the presence of an external magnetic field, the black particles of the magnetic composite GO–Chm were attracted to the wall of the vial to emphasize the magnetism of the prepared GO–Chm.

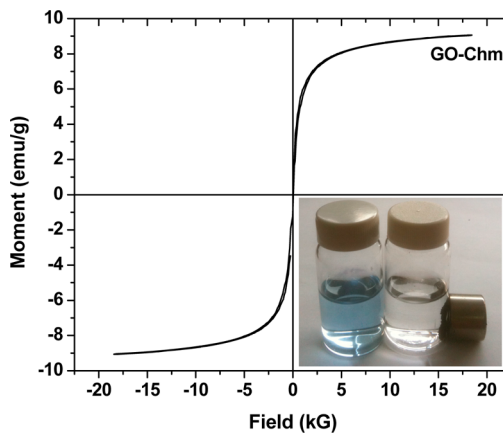


Figure 3. VSM plot of GO–Chm. Inset: Photograph of a magnetic sample of GO–Chm.

Information about the differences in the chemistry of the surfaces can be seen in the differential thermal gravimetry (DTG) curves (Figure 4). The peaks represent weight losses in the specific temperature ranges, and the areas under the peaks are related to the extents of those weight losses. The first peak centered at about 80–100 °C for all samples, in correlation with the endothermic effect on the differential thermal analysis (DTA) curves presented in Figure 5, can be linked to weight loss due to the evaporation of physically adsorbed water. For GO–Chm, this peak presented a maximum at 100 °C. For the GO sample, the second peak presented between 200–250 °C is

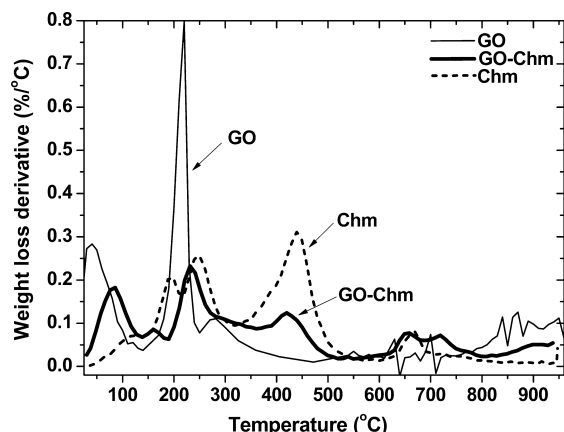


Figure 4. Differential thermogravimetry (DTG) curves obtained in nitrogen.

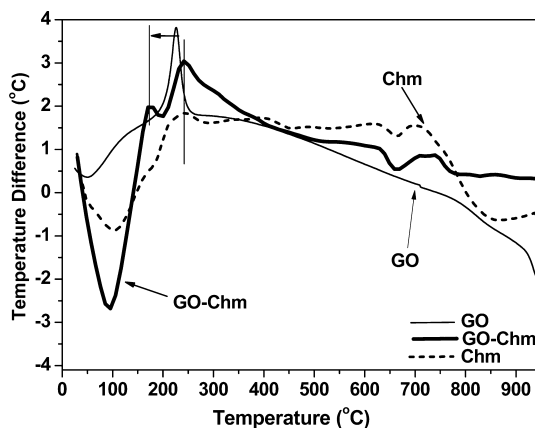


Figure 5. Differential thermal analysis (DTA) curves obtained in nitrogen.

related to the decomposition of epoxy and carboxyl groups,³⁵ which is represented by exothermic peaks on the DTA curve in Figure 5. The shoulder observed between 250–300 °C for GO represents the decomposition of sulfones or the removal of residual sulfuric acid residues after the preparation/oxidation of graphite with sulfuric acid. Chm displays a sharp exothermic peak around 270 °C that can be attributed to the decomposition of chitosan derivatives containing hydroxyl and amino groups. The weight loss in the range 550–610 °C should be assigned to the further decomposition of chitosan residues, whereas the endothermic peak at 759 °C is related to the presence of some amorphous iron oxide.⁴¹ The band in the range of 600–900 °C can be attributed to the reduction of Fe₃O₄ by reaction with residual carbon.⁴²

The DTG curve of GO-Chm presents two peaks with maxima at 150 and 250 °C. The first peak, which is associated with an exotherm in the DTA curves, is related to the decomposition of surface functional groups, accompanied by some degree of exfoliation of the graphene layers.⁴³ The peak is small and occurs at lower temperature than for pure GO. This can be attributed to the fact that most of the graphite oxide was exfoliated/reduced upon reacting with magnetic chitosan, leading to structural disorder, a fact that is coincident with the XRD results.⁴¹ The second peak, which is linked to an exotherm, represents the degradation of chitosan.⁴⁴

The FTIR spectrum of GO (Figure 6, spectrum A) is similar to that previously reported in the literature.^{29,30} Carboxyl

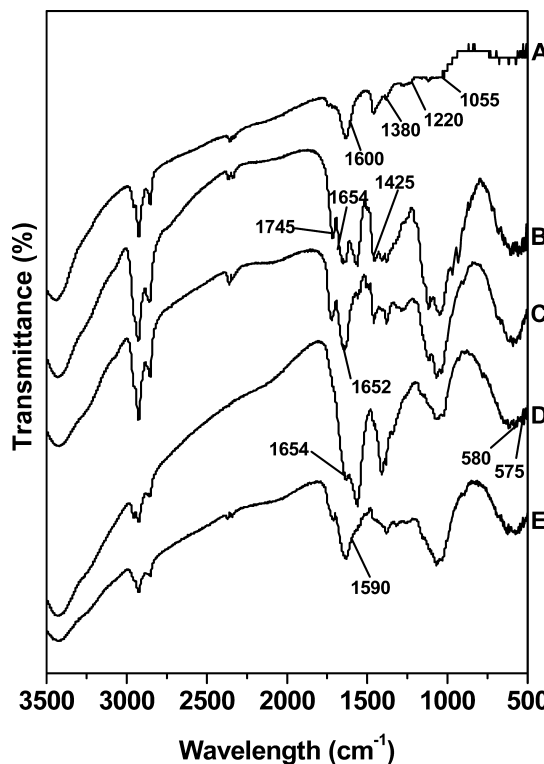


Figure 6. FTIR spectra of (A) GO, (B) Chm, (C) dye-loaded Chm, (D) GO-Chm, and (E) dye-loaded GO-Chm.

groups are observed as bands at 1050–1100 and 1665–1760 cm⁻¹, whereas the band at ~1600 cm⁻¹ is attributed to the presence of epoxy groups³⁵ and the C=C stretching mode of the sp² carbon skeletal network. The peak at 1380 cm⁻¹ and the broad band between 2200 and 3800 cm⁻¹ correspond to O—H groups (C—OH stretching), which either are attached to carbons or represent adsorbed water. The band at 1055 cm⁻¹ can be also attributed to epoxy groups. Another vibration at 1220 cm⁻¹ is also visible, which might arise from S=O asymmetric stretching vibrations in sulfones or sulfates present after graphite oxidation and/or vibrations of C—O groups in epoxides.^{30,45}

The FTIR spectrum of Chm (Figure 6, spectrum B) exhibits characteristic absorption bands of the functional groups of chitosan: at 3200–3400 cm⁻¹ due to the stretching vibration mode of OH and NH₂ group, at 1745 cm⁻¹ due to the C=O stretching in carboxylic acid, at 1654 cm⁻¹ due to the amide I band (C=O stretching mode along with an N—H deformation mode), at 1590 cm⁻¹ due to the NH₂ group, at 1460 cm⁻¹ due to the symmetrical deformation of CH₃ and CH₂ group, at 1425 cm⁻¹ corresponding to C—N axial deformation (amino group band), at 1151 cm⁻¹ assigned to the special broad peak of (1–4)-glucosidic band in polysaccharide unit, at 1096 cm⁻¹ attributed to the stretching vibration mode of the hydroxyl group, at 1028 cm⁻¹ due to the stretching vibration of C—O—C in the glucose circle, and at the 1060–1015 cm⁻¹ corresponding to CH—OH in cyclic compounds.^{17,46} The characteristic peaks at 575 and 580 cm⁻¹ are due to Fe—O deformation in the octahedral and tetrahedral sites of Fe₃O₄.

FTIR spectroscopy is an important technique for understanding the mechanism of a composite's formation, as well as the mechanism of dye adsorption. The spectrum of GO-Chm

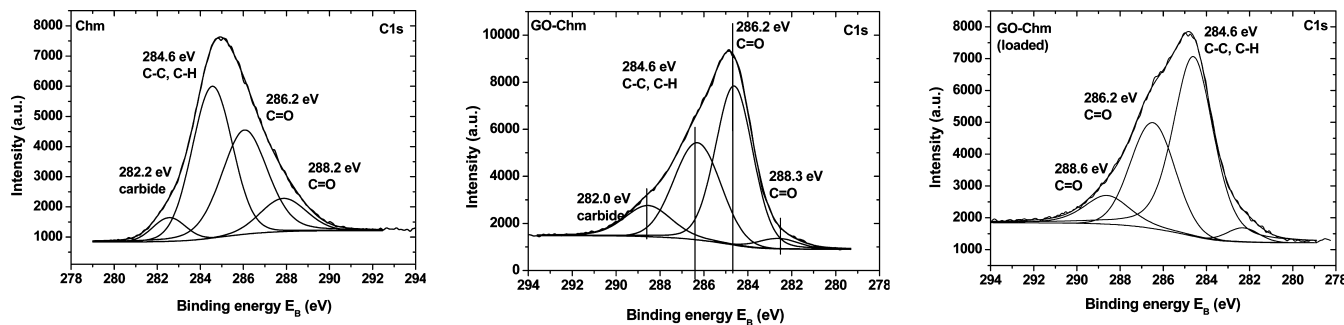


Figure 7. C 1s XP spectra of Chm, GO–Chm, and dye-loaded GO–Chm.

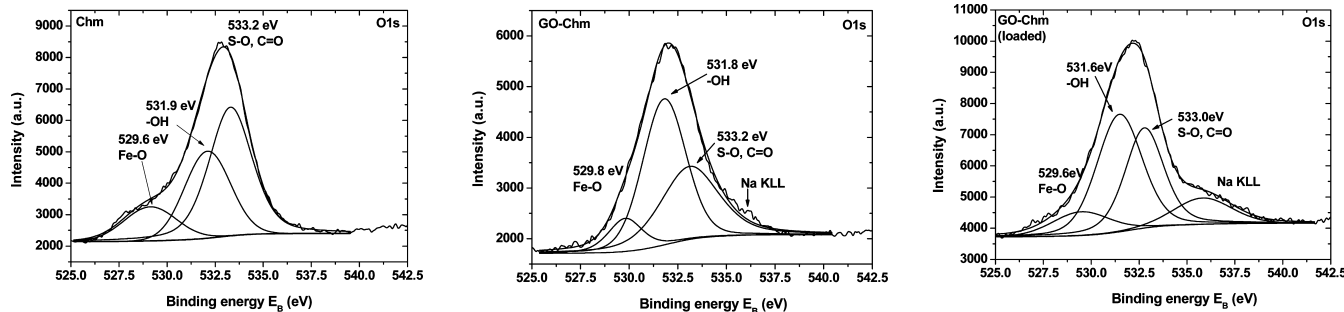
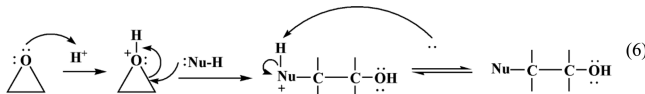


Figure 8. O 1s XP spectra of Chm, GO–Chm, and dye-loaded GO–Chm.

(Figure 6, spectrum D) shows the characteristic peaks of Fe_3O_4 at 575 and 580 cm^{-1} , indicating that Chm was successfully grafted onto GO. Because chitosan has $-\text{NH}_2$ groups on its macromolecular chains, these functional groups can react with oxygen-containing functional groups of GO (carboxyl and epoxy groups) in the following ways: (i) hydrogen–bonding interactions ($\text{G}-\text{OH}\cdots\text{H}_2\text{N}-\text{R}$); (ii) after protonation of the amino by the weakly acidic sites of the GO layers ($-\text{COO}^- + \text{H}_3\text{N}-\text{R}$) with amides and amino carboxylate salts as reaction products, and (iii) after nucleophilic substitution reactions through the attack of the lone pair of amino electrons on the epoxy groups of GO.³¹ Concerning the spectrum of GO–Chm, it can be distinctly observed that the peak at 1730 cm^{-1} , which can be attributed to carboxyl groups, disappeared, confirming that the carboxyl groups reacted with chitosan during the preparation of the composite. In addition, the intensity of the amino absorbance band increased compared to the intensity of the amino group of NHCO (amide I). The amino groups can also react with epoxy functional groups of GO after nucleophilic substitution reactions on the epoxy groups of GO according to the reaction



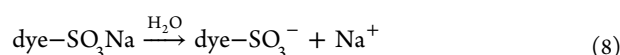
where Nu is the nucleophilic part consisting of amino groups of Ch ($\text{R}_{\text{Ch}}-\text{NH}_2$).

Therefore, we propose as the possible mechanism of the composite formation the reaction of carboxyl groups of GO with amino groups of chitosan to form amides (band at 1636 cm^{-1}) and carboxylate groups (band at $\sim 1400 \text{ cm}^{-1}$), in line with the nucleophilic attack of the amines of chitosan on the epoxy groups of GO (which leads to the amine formation band increase at 1597 cm^{-1}), which are binding sites for dye molecules. The proposed mechanism of the synthesis of GO–Chm is illustrated in Scheme 1.

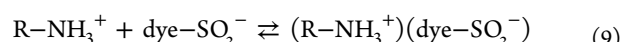
The spectrum of GO–Chm after dye adsorption presents a decrease in the amino peak at 1590 cm^{-1} of loaded adsorbents versus virgin ones (Figure 6, spectra C and E), which confirms the mechanism explaining the interactions between the dye molecules and adsorbents (Chm, GO–Chm). This decrease confirms the binding of the dye molecules to the amino groups of the adsorbent. The amino groups of chitosan (on either Chm or GO–Chm) are protonated under acidic conditions (pH 3) according to the reaction



Simultaneously, the RBS molecule is dissociated^{47,48}



As a result, the main adsorption mechanism proceeds through electrostatic interactions between the two counterions ($\text{R}-\text{NH}_3^+$ and $\text{dye}-\text{SO}_3^-$):^{48,49}



In addition, the presence of Fe_3O_4 nanoparticles and the contribution of GO increase the adsorption ability of magnetic nanocomposite for dye removal. The presence of Fe_3O_4 nanoparticles results in an increased electroactive surface area of Chm or GO–Chm for loading of the dye molecules due to the affinity of the Fe_3O_4 nanoparticles toward the oxygen atoms of RBS. On the other hand, the increased dye adsorption for the GO–Chm composite can be attributed to the contribution of GO through the $\pi-\pi$ dispersion interaction between the aromatic ring of the dye and the GO basal planes. Because of the binding of carboxyl groups to chitosan, these interactions are expected to be stronger. The proposed mechanism of RBS adsorption onto GO–Chm is illustrated in Scheme 1.

To further confirm the previous findings, X-ray photoelectron spectra of Chm, GO–Chm, and dye-loaded GO–Chm were recorded (Figures 8 and 9 and Figure S11 of the

Supporting Information). The binding energies relating to Fe 2p_{3/2} and Fe 2p_{1/2} for all samples were about 711.0 and 724.5 eV, respectively (Figure SI1a, Supporting Information). These binding energies data are consistent with the reported values for Fe₃O₄ in the literature.^{50,51} The N 1s XP spectra of Chm and GO-Chm are reported in Figure SI1b (Supporting Information). C—N from amines or amides (399.8 eV) can be distinguished. Figure 7 shows the deconvoluted C 1s envelopes. The C 1s XP spectrum demonstrates the degree of oxidation with the components to correspond to different functional groups. The first peak at the position of 284.5 eV is assigned to non-oxygenated C (C=C), whereas the second peak at 286.5 eV is assigned to carbons bound to oxygen, as either epoxy or hydroxyl. The third peak at 287.3 is assigned to C=O of alcohols, phenols, or ethers.³⁸ The intensities of the C—O peaks are far diminished from those in GO,³⁸ indicating the deoxygenation of graphite oxide during nanocomposite preparation. The high-resolution O 1s spectra of the samples (Figure 8) were curve-fitted by three peaks: the first peak at 529.8 ± 0.2 eV attributed to Fe—O (Fe₃O₄), the second at 531.8 ± 0.2 eV due to O—H groups, and the third at 533.2 ± 0.2 eV relevant to O—C—O moieties (epoxy, carboxyl groups). The peak attributed to O—H groups increased in the GO-Chm composite, possibly because of hydroxyl formation after the nucleophilic attack of the chitosan amino groups on the epoxy groups of GO, whereas the former peak decreased in the GO-Chm composite because of the reaction of these groups with the amino groups of chitosan. This peak increased in the sample after dye adsorption, possibly because of the cooperation of the S—O groups of the RBS molecule, testifying to the adsorption of the dye on the composite.

3.2. Adsorption–Desorption Evaluation. The prepared composite material was evaluated by a series of experiments as described in section 2.4.

3.2.1. Effect of pH (Adsorption–Desorption). The effect of pH is a key factor of the general so-called adsorption process, which affects both the adsorption of a pollutant onto the material and its desorption from the material into an eluant. Also, pH is directly related to the adsorption mechanism, giving particular explanations for the observed phenomena. Figure 9 illustrates the aforementioned effect. As the majority of previous studies dealt with the removal of anionic (reactive) dyes with chitosan,^{46,47} the adsorption mechanism is strongly influenced by electrostatic interactions between the anionic

(sulfonate) groups of RBS and the cationic groups of the material at acidic pH values. The latter forces can be derived from (i) the amino groups of GO–Chm, which originated from the chitosan matrix or were formed after the breaking of the epoxy groups of GO, or (ii) the amido groups of GO–Chm formed after the interaction of the GO carboxyl groups with the chitosan amino groups. When the pH of the solution is increased, the strong electrostatic forces are weakened, and at alkaline conditions, the adsorption mechanism is mainly attributable to van der Waals bonds or π–π interactions.^{48,49} The pH effect of GO followed the same trend, but with enough lower removal values, given the absence of extra amino groups from the GO network, compared to that of GO–Chm. Another fact that has to be discussed is the relatively high adsorption capability of GO–Chm even under extreme alkaline conditions (pH 12, removal = 35%). This confirms that, under these conditions, the interaction between the already anionic carboxyl groups of GO–Chm and the amino groups of RBS dominate. Another possible interaction is the interaction between the ring of the dye and that of GO–Chm, as illustrated in Scheme 1. In the case of GO–Chm, the quantitative reduction of adsorption with increasing pH was as follows: For pH 3, 4, 6, 8, 10, and 12, removal = 81%, 77%, 70%, 62%, 55%, and 35%, respectively.

The completely opposite phenomenon was revealed with the desorption experiments. When the pH of the eluant was increased, an increase in desorption was observed. This can be explained by the electrostatic nature of the dominant forces in the material–dye system. Weakening of the latter bonds favors dye desorption from the material. At pH 12, the desorption of RBS from GO–Chm was 81%.

3.2.2. Effect of Contact Time (Kinetics). Figure SI2 (Supporting Information) shows the effect of contact time on adsorption. The trend of the curves is similar to those of many other studies reported in the literature.^{47,52,53} For both materials (GO–Chm, GO), the very fast dye removal at the initial stage (0–30 min) implies an external surface diffusion. Then, during the second time period (0.5–3 h), the dye adsorption is milder and more gradual, whereas the last stage (3–24 h) is characterized by the equilibrium state.^{47,52–54} The fast adsorption in the initial stage might be due to the fact that a large number of surface sites are available for adsorption. After a lapse of time, the remaining surface sites are difficult for the dye molecules to occupy because of the repulsion between the solute molecules of the solid and bulk phases, making it take a long time to reach equilibrium. Table 1 presents the kinetic parameters resulting from fits to pseudo-first-order, pseudo-second-order, and modified pseudo-second-order equations to the experimental data. According to the correlation coefficients (R^2), the best fitting was obtained with the modified pseudo-second-order equation (for GO, pseudo-first-order, $R^2 = 0.957$; pseudo-second-order, $R^2 = 0.991$; modified pseudo-second-order, $R^2 = 0.992$; for GO–Chm, pseudo-first-order, $R^2 = 0.847$; pseudo-second-order, $R^2 = 0.972$; modified pseudo-second-order, $R^2 = 0.973$).

It is also worthwhile to comment briefly on the physical significance of the so-called pseudo-first- and pseudo-second-order equations used in the current study. Recent works have not only presented an extensive discussion of the applicability of both pseudo-first- and pseudo-second-order equations, but also, by applying distinct approaches, provided a strong theoretical basis for them, which gives them a clear physical significance.⁵⁵ From all of the cited works, a major conclusion can be drawn, which is the suitability of such equations for

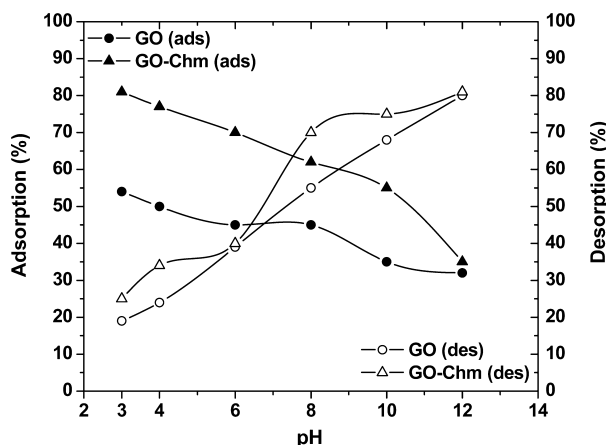


Figure 9. Effect of pH on adsorption and desorption.

Table 1. Kinetic Constants^a for the Adsorption of RBS onto GO and GO-Chm

adsorbent	pseudo-first-order		pseudo-second-order		pseudo-second-order (modified)			
	$C_t = C_0 - (C_0 - C_e) \times (1 - e^{-k_1 t})$	k_1 (min ⁻¹)	$C_t = C_0 - (C_0 - C_e) \times [1 - 1/(1 + k_2 t)]$	k_2 (min ⁻¹)	R^2	$C_t = C_0 - (C_0 - C_e) \times [1 - 1/(b_m + k_{2,m} t)]$	$k_{2,m}$ (min ⁻¹)	b_m
GO	2.440	0.957	3.811	0.991	4.090	0.979	0.992	
GO-Chm	1.940	0.847	3.255	0.972	3.221	1.021	0.973	

^a k_1 , k_2 , and $k_{2,m}$ (min⁻¹) are the rate constants for the pseudo-first-, pseudo-second-, and pseudo-third-order kinetic models, respectively; b_m is the initial surface coverage; and C_0 , C_t , and C_e (mg/L) are the initial, transient, and equilibrium concentrations of dye, respectively, in the aqueous solution.

either long or short times of adsorption, in the case of the pseudo-first- and pseudo-second-order equations, respectively. In other words, during the initial time periods of adsorption (far from equilibrium), the kinetics are governed by the rate of surface reactions, and when the system approaches equilibrium, a switch takes place in the predominant mechanism from surface reactions to intraparticle diffusion.⁴⁶

3.2.3. Isotherms, Thermodynamics. Figure 10 presents the isotherm curves of GO and GO-Chm. Also, Table 2 reports all isothermal parameters resulting from the fitting of the experimental data to the Langmuir, Freundlich, and Langmuir–Freundlich (L–F) models. For RBS removal, Q_{\max} at 25 °C was 221 mg/g for GO (pH 3) and 391 mg/g for GO-Chm

(pH 3). Therefore, the functionalization of GO with Chm impressively improved the Q_{\max} value (GO-Chm) by ~75%. For all of the adsorbents studied, the equilibrium dye uptake was affected by the initial dye concentration using a constant dosage of adsorbent (1 g/L). At low initial concentrations, the dye adsorption was very intense and reached equilibrium rapidly. This phenomenon indicates the possibility of forming monolayer coverage of dye molecules on the outer interface of the material. For low concentrations (0–50 mg/L), the ratio of the initial number of dye molecules to the available adsorption sites is low, and subsequently, the fractional adsorption becomes independent of initial concentration.⁴⁹ In addition, the effect of temperature on equilibrium was also studied and presented through isotherm curves (Figure 10). Both GO and GO-Chm indicated the same behavior: When the temperature was increased from 25 to 65 °C, an increase in the adsorption capacity (dye uptake) was observed. In particular, the Q_{\max} value of GO increased from 221 mg/g at 25 °C to 286 mg/g at 45 °C and finally to 299 mg/g at 65 °C. Similarly, the Q_{\max} value of the composite material improved from 391 mg/g at 25 °C to 401 mg/g at 45 °C and finally to 425 mg/g at 65 °C. In the last case (65 °C), the difference in Q_{\max} between GO and GO-Chm was ~42%. This increase in adsorption is mainly due to the augmentation of the number of adsorption sites caused by the breaking of some of the internal bonds near the edge of the active surface sites of the material network. Also, it could be due to increased penetration of dye molecules inside the possible surface cavities at higher temperatures or the creation of new active sites.^{56,57}

After the thermodynamic analysis, the values of ΔH° and ΔS° were calculated from the slope and intercept, respectively, of a plot of $\ln(K_c)$ versus $1/T$ ($R^2 > 0.987$, data not shown). All thermodynamic parameters, at selected concentrations and all temperatures, are reported in Table SI1 (Supporting Information). Based on thermodynamic theory, the positive values of ΔH° suggest the endothermic nature of the adsorption process. The negative values of ΔG° suggest that the process is spontaneous with high preference for dye molecules. Because the adsorption is endothermic, the amount adsorbed at equilibrium is increased with increasing temperature. The positive values of ΔS° show the increased randomness at the solid/liquid interface. During adsorption, the coordinated water molecules, which are displaced by the dye molecules, gain more translational entropy than is lost by the dye molecules, resulting in increased randomness in the dye–adsorbent interaction.⁵⁸

4. CONCLUSIONS

Synthesis of graphite oxide (GO) with magnetic chitosan (Chm) was achieved to prepare a nanocomposite material (GO-Chm) as an adsorbent material for a dye (Reactive Black

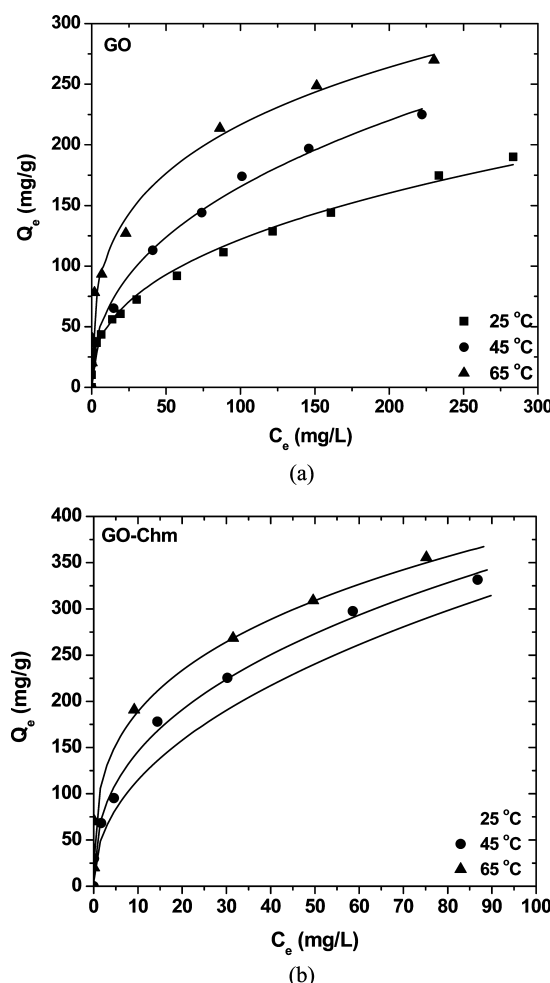


Figure 10. Effect of initial RBS concentration on adsorption onto (a) GO and (b) GO-Chm.

Table 2. Equilibrium Parameters^a for the Adsorption of RB5 onto GO and GO–Chm at 25, 45, and 65 °C

T (°C)	Langmuir equation			Freundlich equation			Langmuir–Freundlich (L–F) equation				
	Q _e = $\frac{Q_{\max} K_L C_e}{1 + K_L C_e}$	K _L (L/mg)	R ²	Q _e = K _F C _e ^{1/n}	K _F (mg ^{1-1/n} L ^{1/n} g ⁻¹)	n	R ²	Q _{max} (mg/g)	K _{LF} [(L/mg) ^{1/b}]	b	R ²
GO Adsorbent											
25	205	0.064	0.931		19.85	2.54	0.984	221	0.022	0.67	0.984
45	269	0.018	0.976		24.08	2.39	0.992	286	0.018	0.64	0.992
65	275	0.018	0.926		52.99	3.29	0.993	299	0.014	0.58	0.993
GO–Chm Adsorbent											
25	368	0.113	0.944		39.99	2.18	0.991	391	0.148	0.60	0.954
45	372	0.067	0.969		59.21	2.56	0.996	401	0.056	0.81	0.970
65	391	0.037	0.976		93.48	3.27	0.989	425	0.030	0.85	0.964

^aQ_e (mg/g) is the equilibrium dye concentration in the solid phase, Q_{max} (mg/g) is the maximum amount of adsorption, K_L (L/mg) is the Langmuir adsorption equilibrium constant, K_F (mg^{1-1/n} L^{1/n} g⁻¹) is the Freundlich constant representing the adsorption capacity, n (dimensionless) is the constant depicting the adsorption intensity, K_{LF} [(L/mg)^{1/b}] is the Langmuir–Freundlich constant, and b (dimensionless) is the Langmuir–Freundlich heterogeneity constant.

5). Various techniques (SEM/EDAX, FTIR spectroscopy, XRD, XPS, DTA, DTG) were used to explain the possible mechanism of synthesis of GO–Chm, in line with the dye–material interactions. In particular, the XRD results indicated that a significant fraction of the amine groups of chitosan were inserted between the GO layers and reacted with the carboxyl and epoxy groups of GO, leading to the reduction of GO and, hence, the destruction of its layered structure. SEM images of GO illustrated its sheetlike structure with a large thickness, smooth surface, and wrinkled edges, whereas Chm presented aggregation and spherical shape. The GO–Chm nanocomposite had a much rougher surface, revealing that many small magnetic chitosan particles had been assembled on the surface of the GO layers with a high density. The confirmation of the success of the chitosan coating and the chemical composition of the Chm and GO–Chm particles were determined by EDX analysis. Information about the differences in the chemistry of the surfaces can be seen in the differential thermal gravimetry (DTG) curves. Also, the interactions of the adsorbent–dye system were confirmed by FTIR spectroscopy through the shifts of the peaks occurring after dye adsorption. The adsorption evaluation of the prepared nanocomposite material showed that acidic conditions were the optimum for the adsorption process (pH 3) and that alkaline conditions (pH 12) were preferable for desorption. Kinetic experiments presented the relatively “fast” adsorption phenomenon and the modified pseudo-second-order equation as the best fitting model. The equilibrium data were fitted to the Langmuir, Freundlich, and Langmuir–Freundlich (L–F) models, calculating the maximum adsorption capacities at 25, 45, and 65 °C (391, 401, and 425 mg/g, respectively). Based on thermodynamic theory, the positive values of ΔH° suggested the endothermic nature of the adsorption process. The negative values of ΔG° suggest that the process is spontaneous with a high preference for dye molecules. The positive values of ΔS° show the increased randomness at the solid/liquid interface upon adsorption of the dye molecules.

ASSOCIATED CONTENT

Supporting Information

Fe 2p and N 1s XP spectra of Chm, GO–Chm, and dye-loaded GO–Chm; figure showing the effect of contact time on the adsorption of RB5 onto GO and GO–Chm; and table with the

thermodynamic parameters for the adsorption of RB5 onto GO and GO–Chm. This material is available free of charge via the Internet at <http://pubs.acs.org>.

AUTHOR INFORMATION

Corresponding Author

*E-mail: lenadj@chem.auth.gr. Tel.: +30 2310 997808. Fax: +30 2310 997859.

Notes

The authors declare no competing financial interest.

ACKNOWLEDGMENTS

The authors gratefully acknowledge Dr. Eleni Pavlidou (Assoc. Professor) and Dr. Orestis Kalogirou (Professor) of the Physics Department of Aristotle University of Thessaloniki of Greece for their aid in the characterization part of this study.

REFERENCES

- (1) Huber, P.; Carré, B. Decolorization of process waters in deinking mills and similar applications: A review. *Bioresources* **2012**, *7*, 1366–1382.
- (2) Forgacs, E.; Cserháti, T.; Oros, G. Removal of synthetic dyes from wastewaters: A review. *Environ. Int.* **2004**, *30*, 953–971.
- (3) Mezohegyi, G.; van der Zee, F. P.; Font, J.; Fortuny, A.; Fabregat, A. Towards advanced aqueous dye removal processes: A short review on the versatile role of activated carbon. *J. Environ. Manage.* **2012**, *102*, 148–164.
- (4) Ramesha, G. K.; Vijaya Kumara, A.; Muralidhara, H. B.; Sampath, S. Graphene and graphene oxide as effective adsorbents toward anionic and cationic dyes. *J. Colloid Interface Sci.* **2011**, *361*, 270–277.
- (5) Ai, L.; Zhang, C.; Chen, Z. Removal of methylene blue from aqueous solution by a solvothermal-synthesized graphene/magnetite composite. *J. Hazard. Mater.* **2011**, *192*, 1515–1524.
- (6) Pei, S.; Cheng, H.-M. The reduction of graphene oxide. *Carbon* **2012**, *50*, 3210–3228.
- (7) Szabó, T.; Berkesi, O.; Forgó, P.; Josepovits, K.; Sanakis, Y.; Petridis, D.; Dékány, I. Evolution of surface functional groups in a series of progressively oxidized graphite oxides. *Chem. Mater.* **2006**, *18*, 2740–2749.
- (8) Szabó, T.; Hornok, V.; Schoonheydt, R. A.; Dékány, I. Hybrid Langmuir–Blodgett monolayers of graphite oxide nanosheets. *Carbon* **2010**, *48*, 1676–1680.
- (9) Szabó, T.; Tombácz, E.; Illés, E.; Dékány, I. Enhanced acidity and pH-dependent surface charge characterization of successively oxidized graphite oxides. *Carbon* **2006**, *44*, 537–545.

- (10) Wang, Y. L.; Gao, P.; Huang, L. H.; Wu, X. J.; Liu, Y. L. Graphite oxide: Preparation and removal ability of cationic dyes. *Chin. J. Inorg. Chem.* **2012**, *28*, 391–397.
- (11) Zhang, W.; Zhou, C.; Zhou, W.; Lei, A.; Zhang, Q.; Wan, Q.; Zou, B. Fast and considerable adsorption of methylene blue dye onto graphene oxide. *Bull. Environ. Contam. Toxicol.* **2011**, *87*, 86–90.
- (12) Crini, G. Recent developments in polysaccharide-based materials used as adsorbents in wastewater treatment. *Prog. Polym. Sci.* **2005**, *30*, 38–70.
- (13) Chen, L.; Wang, T.; Tong, J. Application of derivatized magnetic materials to the separation and the preconcentration of pollutants in water samples. *Trends Anal. Chem.* **2011**, *30*, 1095–1108.
- (14) Sun, H.; Cao, L.; Lu, L. Magnetite/reduced graphene oxide nanocomposites: One step solvothermal synthesis and use as a novel platform for removal of dye pollutants. *Nano Res.* **2011**, *4*, 550–562.
- (15) Zhu, H. Y.; Fu, Y. Q.; Jiang, R.; Yao, J.; Xiao, L.; Zeng, G. M. Novel magnetic chitosan/poly(vinyl alcohol) hydrogel beads: Preparation, characterization and application for adsorption of dye from aqueous solution. *Bioresour. Technol.* **2012**, *105*, 24–30.
- (16) Rinaudo, M. Chitin and chitosan: Properties and applications. *Prog. Polym. Sci.* **2006**, *31*, 603–632.
- (17) Kyzas, G. Z.; Bikiaris, D. N.; Lazaridis, N. K. Low-swelling chitosan derivatives as biosorbents for basic dyes. *Langmuir* **2008**, *24*, 4791–4799.
- (18) Kyzas, G. Z.; Lazaridis, N. K.; Kostoglou, M. Modelling the effect of pre-swelling on adsorption dynamics of dyes by chitosan derivatives. *Chem. Eng. Sci.* **2012**, *81*, 220–230.
- (19) Hummers, W. S., Jr.; Offeman, R. E. Preparation of graphitic oxide. *J. Am. Chem. Soc.* **1958**, *80*, 1339.
- (20) Standard practice for checking the operating characteristics of X-ray photoelectron spectrometers (ASTM E902-88). In *Annual Book of ASTM Standards*; American Society for Testing and Materials: West Conshohocken, PA, 1988.
- (21) Ho, Y. S.; Ng, J. C. Y.; McKay, G. Kinetics of pollutant sorption by biosorbents: Review. *Sep. Purif. Methods* **2000**, *29*, 189–232.
- (22) Langmuir, I. The adsorption of gases on plane surfaces of glass, mica and platinum. *J. Am. Chem. Soc.* **1918**, *40*, 1361–1403.
- (23) Freundlich, H. Over the adsorption in solution. *Z. Phys. Chem.* **1906**, *57*, 385–470.
- (24) Tien, C. *Adsorption Calculations and Modeling*; Butterworth-Heinemann: Boston, 1994.
- (25) Smith, J. M.; Van Ness, H. C. *Introduction to Chemical Engineering Thermodynamics*, 6th ed.; McGraw-Hill: New York, 1987.
- (26) Fan, L.; Luo, C.; Li, X.; Lu, F.; Qiu, H.; Sun, M. Fabrication of novel magnetic chitosan grafted with graphene oxide to enhance adsorption properties for methyl blue. *J. Hazard. Mater.* **2012**, *215–216*, 272–279.
- (27) Seung, H. H. Thermal reduction of graphene oxide. In *Physics and Applications of Graphene—Experiments*; Mikhailov, S., Ed.; InTech: New York, 2011; Vol. 5, pp 73–90.
- (28) Liu, L.; Li, C.; Bao, C.; Jia, Q.; Xiao, P.; Liu, X.; Zhang, Q. Preparation and characterization of chitosan/graphene oxide composites for the adsorption of Au(III) and Pd(II). *Talanta* **2012**, *93*, 350–357.
- (29) Seredych, M.; Petit, C.; Tamashausky, A. V.; Bandosz, T. J. Role of graphite precursor in the performance of graphite oxides as ammonia adsorbents. *Carbon* **2009**, *47*, 445–456.
- (30) Seredych, M.; Tamashausky, A. V.; Bandosz, T. J. Graphite oxides obtained from porous graphite: The role of surface chemistry and texture in ammonia retention at ambient conditions. *Adv. Funct. Mater.* **2010**, *20*, 1670–1679.
- (31) Bourlinos, A. B.; Gournis, D.; Petridis, D.; Szabó, T.; Szeri, A.; Dékány, I. Graphite oxide: Chemical reduction to graphite and surface modification with primary aliphatic amines and amino acids. *Langmuir* **2003**, *19*, 6050–6055.
- (32) Liu, Z. H.; Wang, Z. M.; Yang, X.; Ooi, K. Intercalation of organic ammonium ions into layered graphite oxide. *Langmuir* **2002**, *18*, 4926–4932.
- (33) Dékány, I.; Krüger-Grasser, R.; Weiss, A. Selective liquid sorption properties of hydrophobized graphite oxide nanostructures. *Colloid Polym. Sci.* **1998**, *276*, 570–576.
- (34) Kotov, N. A.; Dékány, I.; Fendler, J. H. Ultrathin graphite oxide–polyelectrolyte composites prepared by self-assembly: Transition between conductive and non-conductive states. *Adv. Mater.* **1996**, *8*, 637–641.
- (35) Seredych, M.; Pietrzak, R.; Bandosz, T. J. Role of graphite oxide (GO) and polyaniline (PANI) in NO₂ reduction on GO-PANI composites. *Ind. Eng. Chem. Res.* **2007**, *46*, 6925–6935.
- (36) Donadel, K.; Felisberto, M. D. V.; Fávere, V. T.; Rigoni, M.; Batistela, N. J.; Laranjeira, M. C. M. Synthesis and characterization of the iron oxide magnetic particles coated with chitosan biopolymer. *Mater. Sci. Eng. C* **2008**, *28*, 509–514.
- (37) Fan, L.; Luo, C.; Lv, Z.; Lu, F.; Qiu, H. Preparation of magnetic modified chitosan and adsorption of Zn²⁺ from aqueous solutions. *Colloids Surf. B* **2011**, *88*, 574–581.
- (38) Li, Y.; Chu, J.; Qi, J.; Li, X. An easy and novel approach for the decoration of graphene oxide by Fe₃O₄ nanoparticles. *Appl. Surf. Sci.* **2011**, *257*, 6059–6062.
- (39) Fan, L.; Luo, C.; Sun, M.; Li, X.; Lu, F.; Qiu, H. Preparation of novel magnetic chitosan/graphene oxide composite as effective adsorbents toward methylene blue. *Bioresour. Technol.* **2012**, *114*, 703–706.
- (40) Hritcu, D.; Humelnicu, D.; Dodi, G.; Popa, M. I. Magnetic chitosan composite particles: Evaluation of thorium and uranyl ion adsorption from aqueous solutions. *Carbohyd. Polym.* **2012**, *87*, 1185–1191.
- (41) Dodi, G.; Hritcu, D.; Lisa, G.; Popa, M. I. Core–shell magnetic chitosan particles functionalized by grafting: Synthesis and characterization. *Chem. Eng. J.* **2012**, *203*, 130–141.
- (42) Rudolph, M.; Erler, J.; Peuker, U. A. A TGA–FTIR perspective of fatty acid adsorbed on magnetite nanoparticles—Decomposition steps and magnetite reduction. *Colloids Surf. A* **2012**, *397*, 16–23.
- (43) Wang, G.; Yang, Z.; Li, X.; Li, C. Synthesis of poly(aniline-co-o-anisidine)-intercalated graphite oxide composite by delamination/reassembling method. *Carbon* **2005**, *43*, 2564–2570.
- (44) Jayakumar, R.; Nagahama, H.; Furuike, T.; Tamura, H. Synthesis of phosphorylated chitosan by novel method and its characterization. *Int. J. Biol. Macromol.* **2008**, *42*, 335–339.
- (45) Layek, R. K.; Samanta, S.; Nandi, A. K. Graphene sulphonic acid/chitosan nanobiocomposites with tunable mechanical and conductivity properties. *Polymer* **2012**, *53*, 2265–2273.
- (46) Kyzas, G. Z.; Kostoglou, M.; Lazaridis, N. K. Relating interactions of dye molecules with chitosan to adsorption kinetic data. *Langmuir* **2010**, *26*, 9617–9626.
- (47) Wong, Y. C.; Szeto, Y. S.; Cheung, W. H.; McKay, G. Equilibrium studies for acid dye adsorption onto chitosan. *Langmuir* **2003**, *19*, 7888–7894.
- (48) Kyzas, G. Z.; Lazaridis, N. K. Reactive and basic dyes removal by sorption onto chitosan derivatives. *J. Colloid Interface Sci.* **2009**, *331*, 32–39.
- (49) Chatterjee, S.; Chatterjee, B. P.; Das, A. R.; Guha, A. K. Adsorption of a model anionic dye, eosin Y, from aqueous solution by chitosan hydrobeads. *J. Colloid Interface Sci.* **2005**, *288*, 30–35.
- (50) Kong, A.; Wang, P.; Zhang, H.; Yang, F.; Huang, S.; Shan, Y. One-pot fabrication of magnetically recoverable acid nanocatalyst, heteropolyacids/chitosan/Fe₃O₄, and its catalytic performance. *Appl. Catal. A: Gen.* **2012**, *417–418*, 183–189.
- (51) Qu, J.; Liu, G.; Wang, Y.; Hong, R. Preparation of Fe₃O₄–chitosan nanoparticles used for hyperthermia. *Adv. Powder Technol.* **2010**, *21*, 461–467.
- (52) Chiou, M. S.; Li, H. Y. Equilibrium and kinetic modeling of adsorption of reactive dye on cross-linked chitosan beads. *J. Hazard. Mater.* **2002**, *93*, 233–248.
- (53) Wong, Y. C.; Szeto, Y. S.; Cheung, W. H.; McKay, G. Pseudo-first-order kinetic studies of the sorption of acid dyes onto chitosan. *J. Appl. Polym. Sci.* **2004**, *92*, 1633–1645.

- (54) Wang, L.; Wang, A. Adsorption properties of congo red from aqueous solution onto N,O -carboxymethyl-chitosan. *Bioresour. Technol.* **2008**, *99*, 1403–1408.
- (55) Franca, A. S.; Oliveira, L. S.; Ferreira, M. E. Kinetics and equilibrium studies of methylene blue adsorption by spent coffee grounds. *Desalination* **2009**, *249*, 267–272.
- (56) Al-Degs, Y. S.; Khraisheh, M. A. M.; Allen, S. J.; Ahmad, M. N. Adsorption characteristics of reactive dyes in columns of activated carbon. *J. Hazard. Mater.* **2009**, *165*, 944–949.
- (57) Crini, G. Non-conventional low-cost adsorbents for dye removal: A review. *Bioresour. Technol.* **2006**, *97*, 1061–1085.
- (58) Unnithan, M. R.; Anirudhan, T. S. The kinetics and thermodynamics of sorption of chromium(VI) onto the iron(III) complex of a carboxylated polyacrylamide-grafted sawdust. *Ind. Eng. Chem. Res.* **2001**, *40*, 2693–2701.